ADVANCED FUNCTIONAL MATERIALS
www.afm-journal.de

Materials Views
www.MaterialsViews.com

Highly Stretchable Conductors Integrated with a Conductive Carbon Nanotube/Graphene Network and 3D Porous Poly(dimethylsiloxane)

Mengting Chen, Ling Zhang, Shasha Duan, Shilong Jing, Hao Jiang, and Chunzhong Li**

Here, a novel and facile method is reported for manufacturing a new stretchable conductive material that integrates a hybrid three dimensional (3D) carbon nanotube (CNT)/reduced graphene oxide (rGO) network with a porous poly(dimethylsiloxane) (p-PDMS) elastomer (pPCG). This reciprocal architecture not only alleviates the aggregation of carbon nanofillers but also significantly improves the conductivity of pPCG under large strains. Consequently, the pPCG exhibits high electrical conductivity with a low nanofiller loading (27 S m^{-1} with 2 wt% CNTs/graphene) and a notable retention capability after bending and stretching. The simulation of the mechanical properties of the p-PDMS model demonstrates that an extremely large applied strain (ε_{appl}) can be accommodated through local rotations and bending of cell walls. Thus, after a slight decrease, the conductivity of pPCG can continue to remain constant even as the strain increases to 50%. In general, this architecture of pPCG with a combination of a porous polymer substrate and 3D carbon nanofiller network possesses considerable potential for numerous applications in next-generation stretchable electronics.

1. Introduction

As one of the key building blocks of next-generation electronics, stretchable conductive materials (SCMs) have become the most attractive motif in materials science and engineering.[1–9] SCMs have considerable advantages over conventional conductors, especially in terms of their high conductivity, large strain endurance (>1%), and exceptional conductivity retention capability during repeated deformations.[10] The outstanding mechanical and electrical properties of carbon nanotubes (CNTs) and graphene have rendered them excellent choices for manufacturing this material through their integration with an elastomeric polymer. However, successfully achieving the superior properties of SCMs has some formidable technological challenges for carbon nano-material/polymer composites. These challenges arise from two major limitations: the difficulty of uniformly dispersing both CNTs and graphene in polymer matrices and the high-performance demands of electrical conductivity without severe deterioration during stretching. First, because of the high aspect ratio and strong π–π interactions among carbon nano-materials, CNTs tend to bundle and aggregate, and graphene sheets are easy to stack in the matrices.[11–13] These processes would all have an adverse impact on the electrical performance of the SCMs. Second, partial breaks and cracks in the conductive networks of matrices are familiar occurrences when the SCMs are stretched to an extremely large strain, for example, 50%.[14] Therefore, the stretching range will be limited to maintain the excellent electrical performance of SCMs for practical applications.

A large number of studies are targeted to addressing these limitations.[15–18] One attractive and efficient method to improve the distribution and dispersion of these carbon nano-materials in SCMs is to construct their three-dimensional (3D) structures in advance and then impregnate them within the polymer.[23] Nevertheless, the commonly used 3D network preparation methods (e.g., organic sol–gel polymerization,[19–21] chemical and hydrothermal reduction,[22,23] and chemical vapor deposition[24,25] are complex, expensive and time consuming. Therefore, although these structures impart the SCMs with high electrical conductivity while maintaining a low nanofiller loading, the large-scale manufacturing of CNTs and/or graphene 3D networks is still largely restricted. Moreover, the electrical conductivities of these 3D carbon nano-material-based polymer composites generally exhibit gradual decreases with increasing strains,[16,17] thereby resulting in significantly reduced conductivities under large strains. For example, in our previous work, the conductivity of a CNT/graphene aerogel/poly(dimethylsiloxane) (PDMS) film exhibited a ≈30% decrease under 30% strain,[16] and a graphene foam/PDMS composite also revealed a 30% decrease under 50% strain.[13] This phenomenon is due to cracking of the conductive network under stretching, which would be more prominent under large deformations. Regarding this point, J. Park et al. provided a new design opportunity for obtaining high electrical conductivity performance from SCMs under large strains from the perspective of the polymer substrate.[18] Their specially designed porous PDMS exhibited a significantly

M. T. Chen, Prof. L. Zhang, S. S. Duan, S. L. Jing, Prof. H. Jiang, Prof. C. Z. Li
Key Laboratory for Ultrafine Materials of Ministry of Education
School of Materials Science and Engineering
East China University of Science and Technology
Shanghai 200237, P. R. China
E-mail: zlingzi@ecust.edu.cn; czli@ecust.edu.cn

DOI: 10.1002/adfm.201401886

© 2014 WILEY-VCH Verlag GmbH & Co. KGaA, Weinheim

improved strain distribution resulting from strut rotations, which imparted the SCM with a constant electrical conductivity even when possessing an extremely deformed geometry. However, the synthesis process has a unique equipment requirement and is not appropriate for thicker composites, rendering the large-scale manufacturing of 3D porous polymer substrates extremely difficult. Therefore, achieving highly conductive SCMs at large scales and at large strains remains a challenge.

Here, we developed a novel strategy for integrating the CNT/graphene conductive network and the 3D porous PDMS substrate. This collaborative structure not only effectively prevents the aggregation of carbon nano-materials but also simultaneously exploits the tensile-endurance property of porous organic stretchable substrates. The 3D porous PDMS (p-PDMS) skeleton is fabricated by replicating the structure of nickel foam, and then, the hybrid CNT/graphene is assembled on this polymer scaffold using the solution impregnation method. The complete process is a facile and inexpensive industrial method for manufacturing SCMs. The electrical conductivity of p-PDMS/CNT/graphene (pPCG) can reach 27 S m^{-1} with only a 2 wt% CNT/graphene loading, corresponding to a remarkable improvement over p-PDMS/CNT (pPC) and p-PDMS/graphene (pPG) composites. This result can be attributed to the superior conductive network formed in the pPCG, which possesses a mutually promoted dispersion of CNTs and graphene.[26,27] The simulation of the mechanical properties of the p-PDMS model demonstrated that a large applied strain (ε_{appl}) can be accommodated through local rotations and bending of cell walls. Meanwhile, the largest strain first emerges and further concentrates on the joints of cell walls, which is typically less than 20% of ε_{appl}. Therefore, the electrical conductivity of pPCG remains constant—after a mild decrease—even when the strain increases to 50%. In general, this collaborative architecture of a 3D porous polymer substrate and carbon nanofiller network provides the pPCG with considerable potential in next-generation stretchable conductors.

2. Preparation and Morphology Analysis of pPCG

Figure 1a illustrates the route for fabricating the pPCG, which includes four main steps. The procedure begins with replicating the Ni foam architecture by dipping the template into a dilute PDMS solution, which is followed by curing and Ni-etching processes. Based on field-emission scanning electron microscopy (FE-SEM) measurements, the thin PDMS layer perfectly copies the 3D network structure of the Ni foam (Figure 1b,c), forming a highly porous framework with continuous macropores. These opened cells occupy the majority of the foam volume, and the surface of p-PDMS is extremely smooth. The average cell width *W*, height *H* and wall width *t* of p-PDMS[28] are calculated in Figure 1e, which have significance for guiding the optimization of the 3D model of p-PDMS used in the finite element analysis (FEA). Because of this special construction, the density of p-PDMS is extremely low ($\rho^* = 0.1$ g cm^{-3}), approximately 10 times lighter than that of the solid polymer ($\rho = 0.965$ g cm^{-3}). Moreover, Figure 1d demonstrates that the p-PDMS is highly stretchable and can be easily stretched to 60% strain without causing any mechanical failure, which makes this polymer material an ideal substrate for SCMs.

Then, the p-PDMS was immersed in a mixed solution of CNTs/graphene oxides (GOs) using a vacuum degassing process. After being dried in an oven and undergoing a subsequent hydroiodic (HI) acid treatment, the reduced GO (rGO) sheets were attracted to each other through strong π–π interactions. These assembled nanofillers tightly attached to the insulting polymer substrate, and they could not be stripped from the substrate, even after ultrasonic treatment for 2 h. The HI acid reduction endows the rGO film with good flexibility while maintaining a considerably higher electrical conductivity and lower probability of structural failure than those of films reduced using other chemical methods (Figure S3, Supporting Information).[29] Finally, the resulting composite was washed with water and directly dried in an oven to yield the pPCG.

The as-prepared pPCG conductive composite exhibits substantially improved electrical properties than p-PDMS-based SCMs formed from pure CNTs (pPC) or graphene (pPG). The results indicated that with the same nanofiller loading (2 wt%), the electrical conductivity of pPCG can reach 27 S m^{-1}, corresponding to an improvement of more than 2 orders of magnitude and 2 times larger than that of pPC and pPG composites (7×10^{-2} S m^{-1} for pPC and 14 S m^{-1} for pPG), respectively. This result could be attributed to the morphologies of these three composites. As shown in **Figures 2**a,b, because of the drastic volume contraction resulting from the evaporation of solvent, the CNTs adhered to the p-PDMS skeletons exhibit a highly entangled morphology with local aggregations. The poor distribution implies the presence of a considerable number of useless contacts among nanotubes and an inferior CNT conductive network, which greatly limits electron transport in the pPC. While, for the pPG composite, Figure 2c,d illustrates that the skeleton has a wrinkled surface, indicating that the graphene

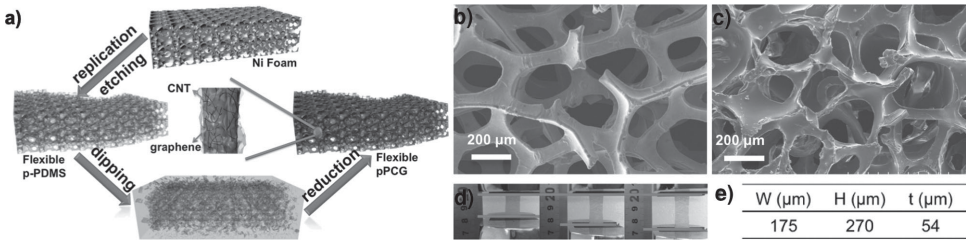

Figure 1. a) Schematic illustration of the pPCG preparation; b,c) FE-TEM images of the Ni foam and p-PDMS, respectively; d) photographs of the p-PDMS substrate, in which the elongation has been measured with a ruler; and e) table reporting the average cell width *W*, height *H* and wall width *t* of p-PDMS.

© 2014 WILEY-VCH Verlag GmbH & Co. KGaA, Weinheim

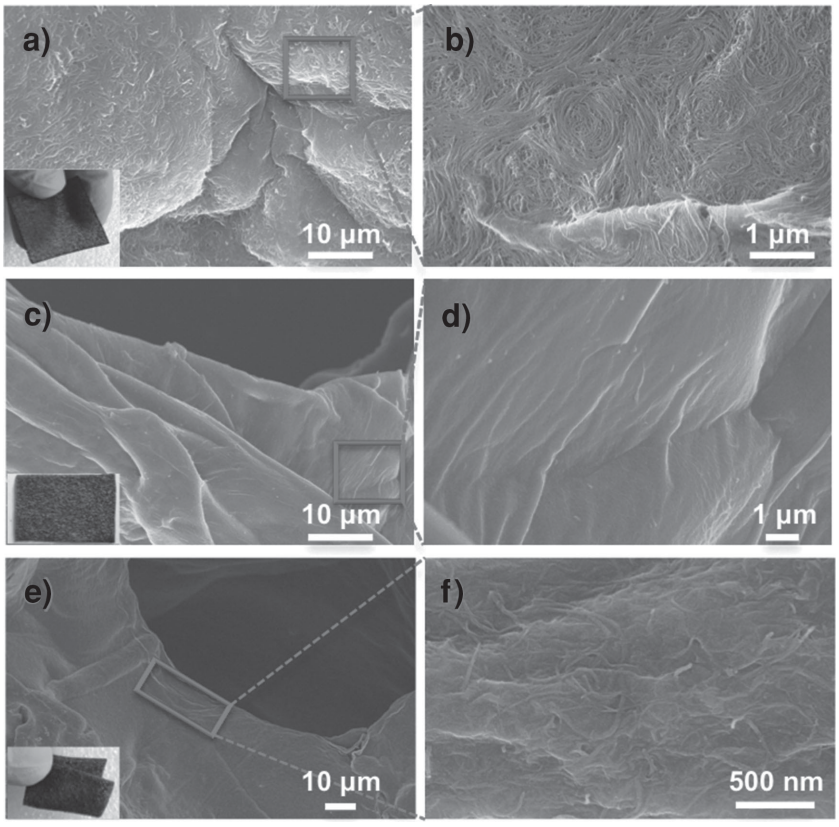

Figure 2. FE-SEM images of the a,b) pPC, c,d) pPG, and c,d) pPCG composites. The insets of (a,c,e) are their corresponding photographs.

sheets completely covered the struts of the p-PDMS substrate. These interconnected and cumulative two-dimensional sheets formed the through-conductive pathway. However, the excessive overlapping of graphene is not conducive for forming the optimal 2D conductive sheets. By contrast, the special architecture of pPCG manufactured from a mixed aqueous solution of CNTs and GO (M_{CNTs}:M_{GO} = 1:1) exhibits a clearly improved nanofiller conductive network. The hybrid CNT/graphene structure effectively alleviates the problems of nanotube aggregation and graphene sheet overlapping; as shown in Figure 2e and f, the graphene sheets can adsorb and disperse pristine CNTs, and similarly, the CNTs act as bridges and prevent the re-stacking of rGO sheets through π–π interactions.[30,31] Therefore, the junctions of the nanotube conductive network and the utilization levels of graphene sheets are both improved remarkably, endowing the pPCG composite with a considerably higher electrical conductivity when its nanofiller concentration is the same as that of the pPC and pPG films.

3. Electrical Properties of the pPCG and Creating the Model of the p-PDMS Structure

3.1. Electrical Conductivity of the pPCG

This specially designed pPCG architecture combines the advantages of both the flexible carbon nanofillers and 3D polymer skeletons, which imparts the composite with both an ultra-high electrical conductivity and excellent electrical properties during the stretching process. As shown in **Figure 3**b, the electrical conductivity (σ) of the pPCG increased as the concentration of CNT/graphene progressively increased. We can clearly observe an abruptly enhanced σ at 0.2 wt% (0.37 S m^{-1}) CNTs/graphene loading in the curve, which indicates that the percolation threshold for the pPCG is extremely small. To determine the applications of the pPCG in stretchable electronics, the pPCG film was stretched to a series of certain preset strains using an electromechanical universal testing machine, and its electrical performance was measured; as shown in Figure 3a, the pPCG exhibits outstanding elasticity and strength, and it can be stretched by more than 80% without causing any mechanical failure. The recorded values are normalized by the initial sample conductivity σ_0 at zero strain (σ/σ_0) as a function of the applied tensile strain. The curve in Figure 3c can be divided into four stages: plateau I (P I), precipitous decline I (PD I), plateau II (P II) and precipitous decline II (PD II). The σ of the pPCG remained constant (P I) as the material was stretched to 5% elongation and then decreased when the strain was further increased from 5% to 15% (PD I). We observed a ~25% decrease in σ/σ_0 at 15% strain for the pPCG film. Interestingly, after this decrease, when the strain of the sample continued to increase (P II), the composite maintained its conductivity value rather than declining further. However, when the pPCG was stretched to more than 50% (PD II), its σ began to decrease again and more rapidly than in the PD I stage. As shown in inset of Figure 3c, the conductivity of the pPCG decreases slightly before 50% strain, and declines rapidly during 50% to 80% elongation. The variations in the brightness of a row of LED lamps during the stretching process are consistent with the change in σ trends (Figure 3d). As shown in Figure 3d, the σ of the pPCG could still maintain the normal brightness of the LED lamps after a 25% decrease (PD I). However, compared to SCMs that consisted of carbon nano-materials in a solid polymer matrix, the electrical performance of the pPCG composite under the stretching process exhibits unique and considerably different results. These experimental data can be quantitatively analyzed through theoretical modeling of the structure of the pPCG and further verified by FEA and detailed FE-SEM images.

3.2. FEA Analysis of p-PDMS Model

Based on Figure 1c, the edge-connectivity (the number of edges that meet at a vertex), Z_e, of the p-PDMS is 4; the face-connectivity (the number of faces that meet at an edge), Z_f, is 3; and

© 2014 WILEY-VCH Verlag GmbH & Co. KGaA, Weinheim

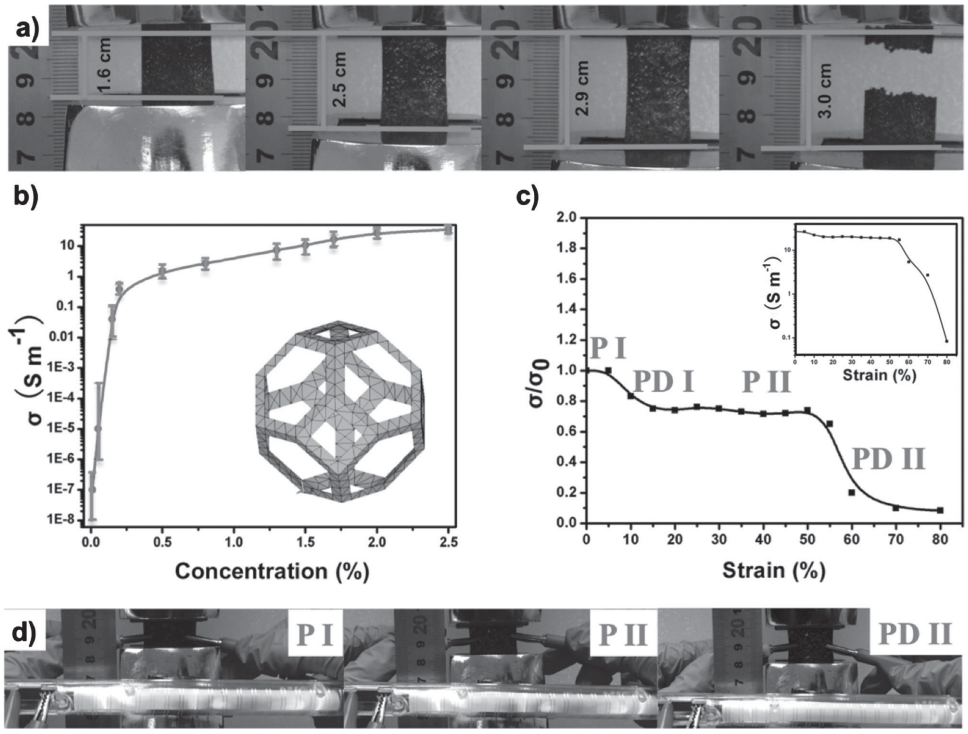

Figure 3. a) Photographs of the pPCG film during the stretching process, in which the elongation is measured with a ruler; b) Conductivity of the pPCG composite with CNTs/graphene loading; c) normalized conductivity of the composite as a function of tensile strain, inset curve shows the electrical conductivity of the pPCG with 2 wt% graphene/CNT loading under stretching; and d) brightness of LED lamps depending on the strains.

the average number of sides per face, n, is approximately 5.2. According to Euler's law,[32]

$$n = \frac{Z_e Z_f}{Z_e - 2}\left(1 - \frac{2}{f}\right)$$

the number of faces (f) is 15. Because the simulations of the mechanical properties of 3D porous elastomers can be expressed using a repeating unit-cell structure, a space-filling geometry is created by repeating itself. Therefore, tetrakaidecahedron, one of the analytical mechanics model proposed by Kelvin in 1887 for bubble formation within foams,[33,34] is used to identify the mechanism of p-PDMS in our work. This model (inset of Figure 3b) has 14 faces and is composed of eight regular hexagons and six squares, which can also be considered as a regular octahedron with six truncated vertices. Consequently, the unit-cell model for p-PDMS is a skeleton structure of tetrakaidecahedron consisting of 24 vertices and 36 edges. Each edge is assumed to be identical, with a cell wall length l and width t. In addition to the local chain arrangement in the polymer, the local strain in the p-PDMS is strongly affected by the pore size because of the unique porous structure of p-PDMS. The value of t/l, which is closely related to the relative density of the foam, is a key element for determining the most appropriate morphology of the model (Figure S8, Supporting Information). Determining the appropriate morphology is critical for precisely simulating the actual deformation of the p-PDMS. The relative density is defined as the ratio of the density of foam (ρ^*) to the density of the material (ρ, the element that constitutes the cell wall). These values can be expressed as follows:

$$\frac{\rho^*}{\rho} = \frac{\frac{\rho V_f}{V}}{\rho} = \frac{V_f}{V} \quad (1)$$

where V_f and V are the volumes of the open-celled p-PDMS framework and tetrakaidecahedron, respectively. The volume of strut joints in the model is small compared to V_f, which can be neglected to simplify the calculation process. Thus, V_f and V can be expressed as follows:

$$V_f = 36Al = 6\sqrt{2}\left(\sqrt{3} - 1\right)t^2 l \quad (2)$$

$$V = V_0 - 6V_t = \frac{\sqrt{2}}{3}(3l)^2 - 6\frac{\sqrt{2}}{3}l^3 = 8\sqrt{2}l^3 \quad (3)$$

where A represents the cross-sectional area of the triangular prism strut. As noted above, V can be calculated as the volume difference between regular octahedron (V_o) and regular tetrahedrons (V_t). Therefore, the relative density of p-PDMS can be expressed as follows:

$$\frac{\rho^*}{\rho} = 0.55\left(\frac{t}{l}\right)^2 \quad (4)$$

The relative density of p-PDMS in our work is approximately 0.1, as shown in Figure 1e, and we defined the value of t as 54 μm. Equation (4) can be used to calculate the value of l as 127 μm. Hence, the geometry of the p-PDMS unit-cell

© 2014 WILEY-VCH Verlag GmbH & Co. KGaA, Weinheim

model can be successfully confirmed, as shown in the inset of Figure 3b. According to literature,[28,35] this regular model is calculated by statistical average value, which can well represent a typical structure of p-PDMS. Thus the general deformation modes of whole porous structure under stretching would be well simulated by only one unit tetrakaidecahedron.

We also simulated the stretching process of a solid polymer cube to highlight and clarify the superior structure of p-PDMS compared to the normal solid polymer. For example, for the 50% strain shown in **Figure 4**c, the solid cube exhibits a more uniformly distributed strain than does the tetrakaidecahedron model. However, ≈47% strain at every point of the solid polymer would induce a stronger effect and damage to the conductive nanofiller network than the p-PDMS. Hence, the highly porous 3D polymer structure is the critical component that endows the pPCG composite with outstanding electrical properties during the stretching process.

The deformation of this porous architecture under stretching was simulated using the finite element method, and the distributions of the strain levels in the models are shown in Figure 4a. When the tetrakaidecahedron is stretched, the cell walls gradually rotate toward the stretching axis. The geometry changes, especially at 50% and 80% elongations, clearly indicate that the strains in the skeletons primarily involve bending strain, which are mainly located at the 36 edges of the model. As shown in Figure 4a, every part of the model exhibits nearly zero strain with 5% elongation (P I stage), and the large structural deformations (greater than the bending strains) first emerge on the joints of the cell walls at 15% strain (the end of the PD I stage) and then gradually increase with increasing strain. When the entire strain of the p-PDMS reaches 50%, ≈3.5%, and ≈10% strains separately impact the edges and vertices of the model. These deformations are multiple times smaller than those at 80% strain, which might explain the formation mechanism of the PD II stage. Therefore, the realistic strains at every location of the cell are comparatively smaller compared with the entire stretching, among which the larger values concentrate on the joints. However, the total area of these joints is far smaller than that of the edges, indicating that the primary deformation mechanism of the cell wall under uniaxial tension is still bending. This result is consistent with the research results presented by W. E. Warren and A. M. Kraynik.[35] In general, the pPCG composite can achieve a large strain via cell wall rotation and small deformations of the skeleton.

The strain distribution maps are more intuitively expressed in Figure 4b. We have summarized five regions on the skeleton of the unit cell, and the average strains in each zone are plotted as a function of the applied strains (ε_{appl}). The deformations on the edges of the model are divided into two categories, zones A and B, which outline the stripes parallel and inclined with an angle

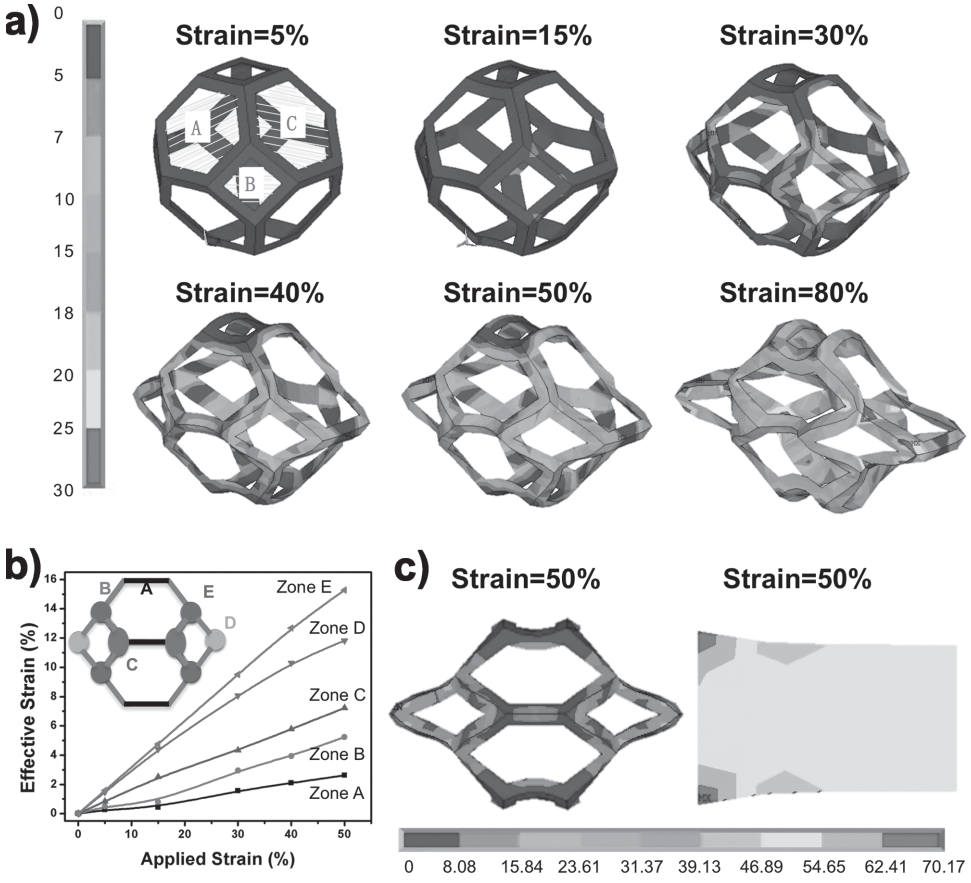

Figure 4. a) The tetrakaidecahedron model of porous p-PDMS under stretching along the X-axis, in which different strain models exhibit clear deformation on each spot of this framework; b) average strains of the tetrakaidecahedron calculated by FEA in the five zones (A to E) as a function of the applied strains; c) comparison of the strain distributions between the porous p-PDMS and solid PDMS models.

© 2014 WILEY-VCH Verlag GmbH & Co. KGaA, Weinheim

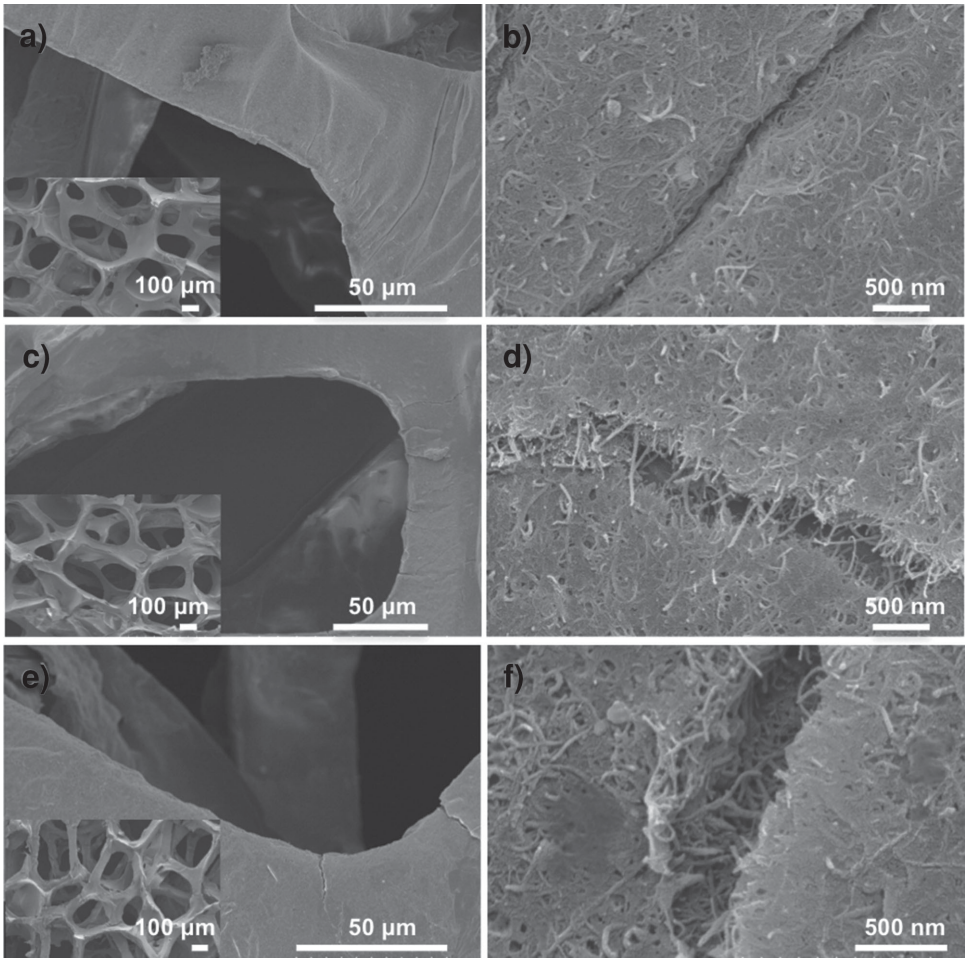

Figure 5. FE-SEM images of the pPCG after stretching: a,b) wrinkles on the surfaces at 5% strain; with further stretching, the wrinkles begin to crack in (c,d) with connected CNTs at 25% strain; the cracks are further deepened at 50% strain in (e,f).

of approximately 45° to the stretching direction, respectively. The similar bending mechanisms in these two types of cell walls are conducive to their relatively small and close strain values despite their distinctly different orientations. The strains in zones A and B are less than 10% of ε_{appl}, and they are not comparable to the deformations in the joint part (zones C to E). This is because each joint in zones C to E is pulled at three curving and rotating stripes. We hypothesize that the different strains in the vertices are strongly affected by the changing of the 3D geometrical shape. During the stretching process, the sizes of faces A and B (marked in Figure 4a) changed slightly, and both changes were accompanied by a movement toward the center of the geometry; consequently, their shapes gradually became concave. However, the shape of face C increasingly evolved to an oblong shape, which reveals an even more striking shape-shifting in the edges of face C than faces A and B. Therefore, the strain in zone C, which is composed of stripes coming from concave faces, is smaller than that in zone D; zones D and E both associate with shape-shifting faces, and the region directly acting as the largest deformation corner of face C (zone E) exhibits a more intense strain than the region (zone D) with less transformation. The strains in the joints are considerably larger than those at the edges, and these strains exhibit a causal relationship with the change in shape under stretching. Thus, we hypothesized that the tightly wrapped conductive network in the p-PDMS would primarily be affected by the relatively larger strains on the vertices.

3.3. Morphology of the pPCG After Stretching

The FE-SEM images of the pPCG after stretching further validate the feasibility of the theoretical model. The adhesive force between the CNT/graphene conductive layer and p-PDMS is extremely strong and stable due to the capillary action produced in the process of impregnation and drying. Therefore, the nanofillers would not flake or peel, even after 2 h of ultrasonic processing, indicating that the load can be effectively transferred from the CNT/graphene layer to the polymer substrate. **Figure 5** depicts the micro-morphologies of the pPCG composites after stretching to a series of preset strains, which recorded the structure changes in the conductive networks with different deformations. Consistent with the geometry changes in the model under stretching, the evident topography variation occurred primarily in the corners of the stripes (Figure 5a,c,e).

© 2014 WILEY-VCH Verlag GmbH & Co. KGaA, Weinheim

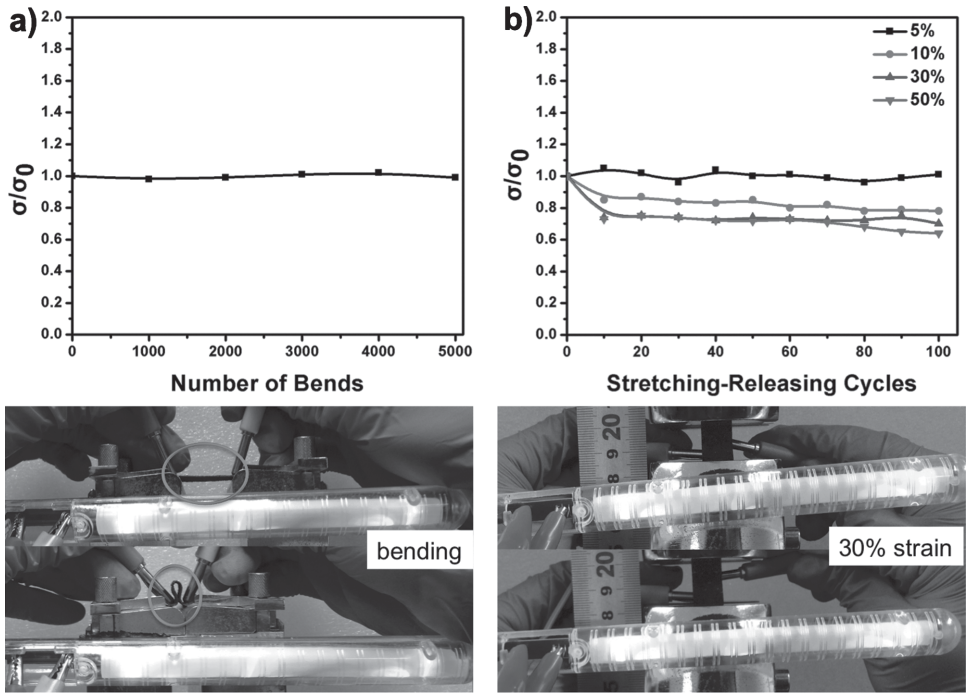

Figure 6. Normalized electro-conductivity of the pPCG as a function of a) the number of bends and b) the stretching-releasing cycles at 5%, 10%, 30%, and 50% strains, respectively. The brightness of LED lamps depending on the bends and strains are shown below the curves.

When the elongation of the sample only reached 5%, as shown in Figure 5a and b, wrinkles and folds appeared densely at joints without any breakage (Figure 5a). This result illustrates that the entire deformation on the struts of the substrate is sufficiently small that the nanofillers can accommodate the applied strain only by extending themselves (concentrating at the corner of the stripes), significantly maintaining the completeness of the conductive pathway (Figure 3c). Subsequently, the pPCG was further stretched to 10% (Figure S9, Supporting Information), and as indicated in Figure 4b, the average strains on the joints increased to around 2%. Under this condition, some regions of the plicated surface began to experience rupture, and thus, the electrical conductivity decreased. As the strain continued to increase to, for example, 25% strain, a large amount of cracks at the corner sprung up and became noticeable (Figure 5c). However, the special architecture constructed by the synergistic nanotubes and graphene sheets has many advantages, including the mutually promoted dispersion of these nanofillers and the characteristic bridging function of one-dimensional (1D) nanotubes to two-dimensional (2D) graphene flakes. Thus, although parts of the 2D sheets fractured under stretching, the CNTs in the interlayer would slide out from one side to another side of graphene similar to bridges (Figure 5d). The disruption of the conductive pathway could be greatly relieved. Then, the pPCG composite was further stretched to 50% strain, and the cracks on surface increased slightly in depth, as shown in Figure 5e. The upper hybrid carbon nano-materials were split open, exposing an intertwined root structure, which confirmed that the consistence of the conductive pathway is largely retained (Figure 5f). This phenomenon is associated with the mode of porous polymer deformation – a large portion of the applied large strain can be neutralized through edge rotation and bending. It is overly complicated to calculate the degree to which the conductive layer shares responsibility for the applied strain; nevertheless, we observed a rapid decrease in the electrical conductivity of the pPCG after 50% strain (Figure 3c) and a complete rupture of the nanofiller layer at 80% strain (ESI). It is hypothesized that ~10% strain at the polymer corners might have already exceeded the ultimate load of the CNT/graphene network. Overall, the unique porous polymer substrate provides not only a 3D template for constructing carbon nano-material networks at low concentration but also a large load bearing and transferring ability to remarkably improve the electrical performance of the composite.

4. Electrical Properties of the pPCG After Cyclical Deformation

The effects of cyclical bending and stretching on the electrical conductivity of the pPCG composite were also studied, as shown in **Figure 6**. As we analyzed and summarized above, the 3D CNT/graphene networks on the porous polymer could maintain their intact pathway after bending and mild stretching deformations. Therefore, Figure 6a,b illustrate that the electrical conductivity of the composite remained constant during 5000 bendings and 100 cycles of a 5% stretching-releasing process. Moreover, the electrical performances of the pPCG at 10%, 30%, and 50% strains after the stretching-releasing cycles yield rational results: its electrical conductivity sustains a value of ≈80%, ≈75%, and ≈75% of the initial values, respectively. However, when the stretching-releasing process enters the final 20 cycles, the electrical conductivity of the composite exhibits

© 2014 WILEY-VCH Verlag GmbH & Co. KGaA, Weinheim

slight decreases at strains of 10%, 30%, and 50%. This phenomenon is presumably due to the mild loosening and fatigue of the attached CNT/graphene layer after dozens of elongations. In general, the overall electrical conductivity retention rate of the composite remained stable during mechanical deformations. The brightness and color of LED lamps remained unchanged after the pPCG was bent to a curvature of 2.5 mm and stretched to 30% strain, which further supports the results described in the σ/σ_0–bending and σ/σ_0–stretching curves (Figure 6a,b). These results indicate that the pPCG composites are suitable for various applications in next-generation SCMs, especially with respect to applications that require outstanding bending and stretching durability.

5. Conclusion

In summary, we have manufactured an integrated 3D porous CNT/graphene and p-PDMS composite with excellent electrical performance. The p-PDMS is fabricated simply by replicating the structure of nickel foam and does not require a sophisticated process. Then, the hybrid CNT/graphene is effectively assembled on the strut walls, forming a 3D network structure with a low loading of conductive nanofillers. The electrical conductivity of the pPCG reaches 27 S m^{-1} with only 2 wt% CNTs/graphene, and this value remained constant after bending 5000 times and after 100 cycles of a 5% stretching-releasing process. Moreover, during the stretching process, the σ of the pPCG first remained unchanged (0–5% strains), and then, after a slight decrease, the σ of the pPCG remained invariant again to up to 50% strain. These phenomena could be quantitatively identified by simulating the mechanical properties through theoretical modeling of p-PDMS. The FEA demonstrates that the large ε_{appl} can be accommodated by rotations and bending of cell walls, and the largest deformations appeared primarily on the joints of struts. The FE-SEM images of the pPCG that had been stretched to a series of strains provided consistent results, which further validated the feasibility of the theoretical model. In addition, the stretchable composite exhibits excellent cyclic electrical properties. When the composite was stretched to 10% and 50%, the σ of the pPCG only decreased by 20% and 25%, respectively, during the first stretching process and then remained unchanged during the remainder of the stretching-releasing cycles. In brief, the strategy provides a facile, inexpensive and simple industrial method for manufacturing a novel SCM that shows many fascinating properties for applications in stretchable next-generation electronics.

6. Experimental Section

Experimental Details: Graphene oxide (GO) and hydrophilic multi-walled carbon nanotubes (t-MWCNTs) were fabricated using a modified Hummers method and a mixed acid treatment, respectively, as reported in our previous work.[23,24] A mixed aqueous solution of these two carbon nano-materials (4 mg mL^{-1}) was prepared with a 1:1 t-MWCNTs:GO mixing ratio and was uniformly dispersed using an ultrasonic cell disruptor (model JY96-II, sonic power ≈ 150 W, frequency ≈ 20 kHz, Ningbo Haishu Kesheng Ultrasonic Equipment Co., Ltd., Ningbo, China) for 2 h. The nickel (Ni) foam sample was dipped into a dilute PDMS (SYLGARD 184, Dow Corning) solution for 30 min, which was prepared by mixing the PDMS base agent, curing agent and ethyl acetate in a ratio of 30:3:100. The PDMS solution on the Ni foam framework was cured at 80 °C for 1 h under vacuum (1.3 kPa). Then, the Ni was removed using a ferric nitrate ($Fe(NO_3)_3$) solution (1 M) at 60 °C for 72 h to obtain the porous PDMS (p-PDMS) foam, which was then dried in oven at 40 °C for 24 h. However, the polymer is hydrophobic, which prevents the penetration of the carbon nanofiller aqueous solution. Hence, we adopted the "forced impregnation" method of Gilles Grondin.[36] The highly stretchable polymer substrate was first dipped into ethanol and then submerged into a CNT/graphene solution. By using a vacuum pump, the volatile ethanol was first extracted from the p-PDMS, creating a vacuum inside the substrate, which would drive the full infiltration of the aqueous solution of carbon nanofillers. After drying in oven at 40 °C and then being reduced by HI at 60 °C for 2 h, the highly stretchable conductive pPCG was successfully obtained. The pPC and pPG preparations were the same as those for pPCG, except the conductive solution was changed to CNT and graphene oxide aqueous solutions.

Characterization: The morphologies of p-PDMS and of the carbon nano-material-based polymer composites were examined using a field-emission scanning electron microscope (FE-SEM, Hitachi S-4800) operating at 5 kV. The electrical conductivities of these composites were measured using a four-point probe (model RTS-8, Guangzhou 4Probes Tech Industrial Co., Ltd., Guangzhou, China) contact direct current (DC) conductivity measurement method at room temperature. The tensile tests were performed using a universal testing machine (CMT4204, Sansi Co., Ltd, China).

Supporting Information

Supporting Information is available from the Wiley Online Library or from the author.

Acknowledgements

This work was supported by the National Natural Science Foundation of China (51173043, 21136006, 21236003, 21322607), the Special Projects for Nanotechnology of Shanghai (11nm0500200, 12nm0502700), the Basic Research Program of Shanghai (13JC1408100, 13NM1400801), Program for New Century Excellent Talents in University (NCET-11–0641), the Fundamental Research Funds for the Central Universities.

Received: June 9, 2014
Revised: August 17, 2014
Published online: October 1, 2014

[1] R. F. Service, *Science* **2003**, *301*, 909.
[2] Y. Li, H. Shimizu, *Macromolecules* **2009**, *42*, 2587–2593.
[3] N. Liu, G. Fang, W. Zeng, H. Zhou, H. Long, X. Zhao, *J. Mater. Chem.* **2012**, *22*, 3478–3484.
[4] T. Someya, T. Sekitani, S. Iba, Y. Kato, H. Kawaguchi, T. Sakurai, *Proc. Natl. Acad. Sci. U.S.A.* **2004**, *101*, 9966.
[5] J. L. Vickery, A. J. Patil, S. Mann, *Adv. Mater.* **2009**, *21*, 2180–2184.
[6] I. Khrapach, F. Withers, T. H. Bointon, D. K. Polyushkin, W. L. Barnes, S. Russo, M. F. Craciun, *Adv. Mater.* **2012**, *24*, 2844–2849.
[7] A. S. Patole, S. P. Patole, H. Kang, J.-B. Yoo, T.-H. Kim, J.-H. Ahn, *J. Colloid Interface Sci.* **2010**, *350*, 530–537.
[8] K. Kalaitzidou, H. Fukushima, L. T. Drzal, *Carbon* **2007**, *45*, 1446–1452.
[9] G. Chen, W. Weng, D. Wu, C. Wu, *Eur. Polym. J.* **2003**, *39*, 2329–2335.

© 2014 WILEY-VCH Verlag GmbH & Co. KGaA, Weinheim

[10] D.-H. Kim, J. A. Rogers, *Adv. Mater.* **2008**, *20*, 4887–4892.
[11] M. K. Shin, J. Oh, M. Lima, M. E. Kozlov, S. J. Kim, R. H. Baughman, *Adv. Mater.* **2010**, *22*, 2663–2667.
[12] N. Grossiord, J. Loos, L. Van Laake, M. Maugey, C. Zakri, C. E. Koning, A. J. Hart, *Adv. Funct. Mater.* **2008**, *18*, 3226–3234.
[13] T. Sekitani, Y. Noguchi, K. Hata, T. Fukushima, T. Aida, T. Someya, *Science* **2008**, *321*, 1468–1472.
[14] Z. Chen, W. Ren, L. Gao, B. Liu, S. Pei, H.-M. Cheng, *Nat. Mater.* **2011**, *10*, 424–428.
[15] M. Chen, L. Zhang, S. Duan, S. Jing, H. Jiang, M. Luo, C. Li, *Nanoscale* **2014**.
[16] M. Chen, T. Tao, L. Zhang, W. Gao, C. Li, *Chem. Commun.* **2013**, *49*, 1612–1614.
[17] K. H. Kim, M. Vural, M. F. Islam, *Adv. Mater.* **2011**, *23*, 2865–2869.
[18] J. Park, S. Wang, M. Li, C. Ahn, J. K. Hyun, D. S. Kim, D. K. Kim, J. A. Rogers, Y. Huang, S. Jeon, *Nat. Commun.* **2012**, *3*, 916.
[19] M. A. Worsley, S. O. Kucheyev, J. D. Kuntz, A. V. Hamza, J. H. Satcher Jr., T. F. Baumann, *J. Mater. Chem.* **2009**, *19*, 3370.
[20] M. A. Worsley, P. J. Pauzauskie, T. Y. Olson, J. Biener, J. H. Satcher Jr., T. F. Baumann, *J. Am. Chem. Soc.* **2010**, *132*, 14067–14069.
[21] M. A. Worsley, S. O. Kucheyev, H. E. Mason, M. D. Merrill, B. P. Mayer, J. Lewicki, C. A. Valdez, M. E. Suss, M. Stadermann, P. J. Pauzauskie, J. H. Satcher, J. Biener, T. F. Baumann, *Chem. Commun.* **2012**, *48*, 8428.
[22] H. Hu, Z. Zhao, W. Wan, Y. Gogotsi, J. Qiu, *Adv. Mater.* **2013**, *25*, 2219–2223.
[23] Y. Xu, K. Sheng, C. Li, G. Shi, *ACS Nano* **2010**, *4*, 4324–4330.
[24] E. Singh, Z. Chen, F. Houshmand, W. Ren, Y. Peles, H.-M. Cheng, N. Koratkar, *Small* **2012**, *9*, 75–80.
[25] M. T. Pettes, H. Ji, R. S. Ruoff, L. Shi, *Nano Lett.* **2012**, *12*, 2959–2964.
[26] R. K. Paul, M. Ghazinejad, M. Penchev, J. Lin, M. Ozkan, C. S. Ozkan, *Small* **2010**, *6*, 2309–2313.
[27] X. Sun, H. Sun, H. Li, H. Peng, *Adv. Mater.* **2013**, *25*, 5153–5176.
[28] H. Vandeparre, Q. Liu, I. R. Minev, Z. Suo, S. P. Lacour, *Adv. Mater.* **2013**, *25*, 3117–3121.
[29] T.-K. Hong, D. W. Lee, H. J. Choi, H. S. Shin, B.-S. Kim, *ACS Nano* **2010**, *4*, 3861–3868.
[30] C. Zhang, L. Ren, X. Wang, T. Liu, *J. Phys. Chem. C* **2010**, *114*, 11435–11440.
[31] C. Zhang, S. Huang, W. W. Tjiu, W. Fan, T. Liu, *J. Mater. Chem.* **2012**, *22*, 2427–2434.
[32] L. J. Gibson, M. F. Ashby, *Cellular Solids: Structure and Properties*, Cambridge University Press, UK **1999**, 30–33.
[33] Y. Kwon, R. Cooke, C. Park, *Mater. Sci. Eng. A* **2003**, *343*, 63–70.
[34] L. Xie, K. Chan, *Int. J. Mech. Sci.* **2006**, *48*, 249–255.
[35] a) Y. Yu, J. Zeng, C. Chen, Z. Xie, R. Guo, Z. Liu, X. Zhou, Y. Yang, Z. Zheng, *Adv. Mater.* **2014**, *26*, 810–815; b) W. Warren, A. Kraynik, *J. Appl. Mech.* **1988**, *55*, 341–346.
[36] G. Grondin, *J. Can, Chiropr. Assoc.* **1998**, *42*, 107–112.

© 2014 WILEY-VCH Verlag GmbH & Co. KGaA, Weinheim